Multifunctional covalent organic framework membranes with an ultrathin recycled palladium nanolayer for efficient water decontamination

Shaochong Cao [a], Dongyang Li [a], Adam A. Uliana [b], Yuanli Jiang [c], Junyong Zhu [a,*], Yatao Zhang [a,d,**], Bart Van der Bruggen [e]

[a] School of Chemical Engineering, Zhengzhou University, Zhengzhou 450001, China
[b] Department of Chemical and Biomolecular Engineering, University of California, Berkeley, CA 94720, USA
[c] Chemical Research Institute, Research Institute of Henan Energy and Chemical Industry Group, Zhengzhou 450046, China
[d] Engineering Research Center of Advanced Manufacturing of Ministry of Education, Zhengzhou University, Zhengzhou 450001, China
[e] Department of Chemical Engineering, KU Leuven, Celestijnenlaan 200F, B-3001 Leuven, Belgium

ABSTRACT

Palladium recycling offers a sustainable and economic approach to meet the rising global demand of this precious yet naturally scarce metal. Here, we demonstrate a new recovery concept that utilizes a bipyridine-based adsorptive membrane (AM) based on covalent organic frameworks (COFs). This approach enables selective recovery of palladium via local coordination and electrostatic interaction, followed by in situ reduction to form a palladium nanolayer within the COF AM. Simulation and experimental results demonstrate that palladium nanoparticles with narrow size distributions were evenly enriched and localized within the continuous, 33-nm-thick COF nanofilm. This palladium enrichment step further provided high catalytic activity (99.9 % conversion of 4-nitrophenol) to the nanofilms, which maintained an ultrahigh water permeability (226.0 L m^{-2} h^{-1} bar^{-1}). These multifunctional properties outperform state-of-the-art catalytic membranes. This study opens new directions in recovering and repurposing palladium waste into catalytic membranes, using COF membranes that efficiently decontaminate water.

1. Introduction

Palladium (Pd) has been increasingly utilized as a precious metal in electronic devices [1], industrial catalysts [2,3], and ceramic capacitors [4]. This metal offers favorable properties such as high catalytic and conductive behavior [5], superior chemical stability [6], and durable corrosion resistance [7]. However, the abundance of Pd in the earth's crust is only 0.1–3 ng g^{-1} [8], and the continuous and rapid industrial consumption of Pd has increased the amount of worldwide Pd-containing solid waste (e.g., inactivated catalysts, electronic waste) [9]. This drastic imbalance between Pd supply and demand prevents a circular economy and sustainable development [10]. Improved technologies that can effectively recycle Pd waste are essential to supply a secondary Pd source, reduce dependence on Pd supply from natural reserves, and alleviate the adverse environmental effects induced by Pd-based waste.

Palladium recovery from solid waste is most typically performed by first dissolving the waste and converting Pd(0) into $PdCl_n^{x-}$ (n = 1, 2, 3, 4, x = n-2), using strong acids with chlorine gas [11]. The low-concentration palladium must then be selectively captured in the presence of diverse ion mixtures (e.g., Cl^-, NO_3^-, Ni^{2+}, Cu^{2+}). While stripping solid waste materials that contain precious palladium for resource recovery has been achieved by hydrometallurgical methods (e. g., extraction, ion exchange, co-precipitation), the harsh chemical processing means and high cost necessitate the exploration of more sustainable and ecofriendly approaches [12,13]. By contrast, adsorption represents a promising alternative for selective capture of precious palladium due to the advantages of reducing adverse environmental effect, ease of operation, and can exhibit heightened selectivity performance [14]. To treat Pd-containing acid exudate, absorbents must be chemically stable, feature a strong affinity to $PdCl_n^{x-}$, and attain high Pd adsorption capacity and selectivity.

Covalent organic frameworks (COFs) are a category of porous absorbents that feature a high surface area, a strong chemical stability, and

---

a customizable pore structure [15–20]. COFs bearing specific functional groups (e.g., thioether, phosphine, allyl) that interact with Pd were rationally developed and utilized for the selective adsorption of palladium [21–24]. Although the resulting Pd(II)@COF nanocomposites have potential usage in catalysis, a rapid depletion of palladium renders them difficult to be used for industrial applications. In addition, the form of COF powders inevitably complicates the subsequent purification and recycling process, probably weakening the practical concept of repurposing the palladium by using COF powders [25]. Instead, an adsorptive membrane (AM) that features ion-capture traits and high reusability offers a promising solution to recover valuable metals [26,27]. Likewise, COF-based AMs have extraordinary adsorption capacities because of their porous structure and designable adsorption sites, that allow higher functional group densities, while having the benefit of minimizing separation steps. On the other hand, in situ growth of palladium nanoparticles on COF membranes via chemical reduction of Pd(II) to Pd(0) is highly effective to eliminate the risk of rapid ion leakage. The presence of strong anchoring sites uniformly spread throughout the COF-based AMs is expected to facilitate confined growth of Pd nanoparticles, yielding narrowly distributed nanoparticles with minimal aggregation [28,29]. In this manner, we envision that COF-based AMs serving as an integrated adsorbents could have enormous potential to convert the captured precious Pd ions into catalytic Pd nanoparticles, forming COF-based catalytic membranes (CMs).

Herein, we propose the concept of using chemically stable COF-based AMs to selectively capture precious palladium from acidic extrusion waste materials. We demonstrate that the synthesized bipyridine-based TpBpy COF membranes can capture $PdCl_4^{2-}$ in simulated acid wastewater (pH = 2.5) with minimal capture of competing ions (SO_4^{2-}, NO_3^-, Cl^-, Ni^{2+}, Na^+). This selectivity is mainly ascribed to local coordination, electrostatic, and hydrogen interactions between the bipyridine anchoring sites and $PdCl_4^{2-}$. Subsequently, in situ growth of captured palladium via chemical reduction yields highly dispersed palladium nanoparticles enriched and localized in COF nanofilms, forming a thin nanolayer of recycled palladium nanoparticles. The resulting catalytic membranes (Pd-TpBpy) were applied for catalytic conversion of toxic 4-nitrophenol (4-NP) into 4-aminophenol (4-AP) with reductant NaBH₄. As a typical toxic nitroaromatic contaminant, 4-NP is extensively used in the processes of chemically producing dyes, leather preservatives, and drug intermediates. The discharge of toxic 4-NP to surface waters and soil poses severe damage to humans, animals, and plants [30]. The reduction of nitroaromatic to an aromatic amine with metal catalysis is an effective strategy, as aromatic amines are a factor 500 less toxic than their corresponding nitroaromatics [31,32]. Two membrane catalytic modes (static catalysis and dynamic catalysis) were designed and compared, with dynamic catalysis mode showing a higher efficiency (99.9 % conversion rate) in a continuous process than in static catalysis mode (96.5 % conversion rate, 125 min). Furthermore, we show that these Pd-recycled COF membranes offer promising antibacterial activity against *E. coli.* This proof-of-concept report paves a new path of upcycling of palladium waste using multifunctional COF adsorptive membranes for additional potential use in catalysis-assisted water decontamination.

2. Experimental section

2.1. Fabrication of TpBpy adsorptive membranes (TpBpy AMs)

As shown in Fig. S1, TpBpy adsorptive membranes were fabricated via the in-situ interfacial polymerization (IP) process between 1,3,5-triformyl phloroglucinol (Tp) and 5,5′-diamino-2,2′-bipyridine (Bpy). Firstly, the wetted polyacrylonitrile (PAN) porous substrate was fixed onto a custom-made membrane module, and the surface water was gently swept using an air knife. Then, a 7 mL aqueous solution containing Bpy (0.15 w/v%) and 0.05 mL AcOH was gently dropped onto the PAN support, which was then left undisturbed for 3 min before the

residual solution was gently swept using an air knife. A 7 mL Tp hexane solution (0.1 w/v%) was then gently poured onto the Bpy-saturated substrate before drained off after 3 min. Finally, the resulting adsorptive membranes were further subjected to thermal treatment at 70 °C for 3 min to enhance the adherence between the TpBpy and PAN substrate. The membranes were stored in DI water before use.

2.2. Palladium(II) recovery performance

2.2.1. Pd(II) sorption kinetics

A Pd(II) stock solution (20 mg/L) was prepared using Na₂PdCl₄, with the solution pH adjusted to 2.5 using hydrochloric acid. One piece of the TpBpy AMs (2×2 cm²) was immersed in a 20 mL Pd(II) stock solution. Subsequently, the solution was placed in a thermostatic shaker at 25 °C and 121 rpm. The residual Pd(II) content was recorded at different time intervals using UV-Vis spectroscopy (Shimadzu, UV-1800, Japan). The Pd-saturated membrane was denoted as Pd(II)-TpBpy.

2.2.2. Pd(II) sorption isotherms

One piece of the TpBpy AMs (2 cm × 2 cm) was soaked in 20 mL of different concentrations of Pd(II) solution (pH 2.5). Subsequently, the solution was placed in a thermostatic shaker at 25 °C and 121 rpm for 12 h. The residual Pd(II) content was determined using the UV-Vis spectroscopy.

2.3. Application in simulated leaching liquor

The simulated leaching liquor was prepared by Na₂PdCl₄, Ni(NO₃)₂, Na₂SO₄, MgCl₂, KCl, and CaCl₂. The species and concentrations of ions are determined according to the actual leaching liquor of the palladium-nickel plating plant. The primary components were measured using atomic absorption spectroscopy (AAS) as follows: palladium 20.6, nickel 30.3, sodium 82.0, potassium 16.6, magnesium 7.0, and calcium 16.2 mg/L. After adjusting the pH to 2.5 with concentrated hydrochloric acid, one piece of the TpBpy AMs (2 cm × 2 cm) was immersed in a 20 mL Pd (II) stock solution. The solution was placed in a thermostatic shaker at 25 °C and 121 rpm for 12 h. The residual metal ions contents were tested with atomic absorption spectroscopy (AAS) to determine the remaining Pd(II) content.

2.4. Fabrication of Pd-TpBpy catalytic membranes (Pd-TpBpy CMs)

In a typical procedure, one piece of the Pd(II)-TpBpy CM (4×4 cm²) was placed in a 0.1 mol/L, 200 mL NaBH₄ solution (methanol and water in a volume ratio of 1:1 as mixed solvent) for in situ growth of Pd nanoparticles. After 30 min of reduction, the resulting membranes were stored in DI water before use and were denoted as Pd-TpBpy CMs.

2.5. Catalytic performance

To comprehensively measure the catalytic performance of the Pd-TpBpy CMs, we designed both static and dynamic catalysis.

2.5.1. Static catalysis

Typically, an aqueous solution (pH 9, 20 mL) containing 4-NP (0.3 mmol/L) and NaBH₄ (50 mmol/L) was first prepared. A piece of Pd-TpBpy CM (2×2 cm²) was then introduced to the above aqueous solution in a flask at room temperature. The reaction progress was monitored by using UV-Vis spectroscopy (Shimadzu, UV-1800, Japan). For comparison, the humic acid (HA, 20 ppm) was added to the above solution to evaluate the effect of HA on the membrane catalytic performance. The HA concentration was measured using a total organic carbon (TOC) analyzer (Shimadzu, TOC-L CPN, Japan).

2.5.2. Dynamic catalysis

The Pd-TpBpy CMs were fixed into a cross-flow filtration device

(Fig. 4e, effective membrane radius is 1.5 cm). Then, 4-NP (0.3 mmol/L) and NaBH$_4$ (50 mmol/L) aqueous solution (pH 9) were utilized as the feed. A colorless 4-Aminophenol (4-AP) solution was obtained under 1.5 bar pressure. The reaction is of first order in the concentration of 4-NP, and the apparent rate constant K_{cat} of dynamic catalysis is calculated by Eq. (1):

$$K_{cat} = -\frac{ln(C_P/C_F)}{t} \tag{1}$$

C_P is the permeate concentration of 4-NP and C_F is the feed concentration of 4-NP. t (ms) is the contact time of the feed solution with Pd-TpBpy CMs. In addition, to measure the simultaneous catalysis and rejection performance of the Pd-TpBpy CMs, 20 mg humic acid (HA) was added to the above 1 L solution. The 4-NP concentration in the permeate was also recorded using the UV–Vis spectroscopy. The HA concentration was measured with a total organic carbon (TOC) analyzer (Shimadzu, TOC-L CPN, Japan).(Fig. 1).

3. Results and discussion

3.1. Design, fabrication, morphology and structure of membranes

Bipyridine-containing TpBpy-COF AMs were fabricated onto a porous polyacrylonitrile (PAN) support via an interfacial polymerization (IP) process, where the condensation of Tp and Bpy catalyzed by acetic acid yields a thin COF nanofilm (Fig. S1). Afterwards, TpBpy AMs were employed to capture the PdCl$_4^{2-}$ from simulated extrusion waste, and turned into Pd-TpBpy CMs via in situ growth of palladium nanoparticles. The chemical structure of as-fabricated membranes was characterized by ATR-FTIR spectroscopy (Fig. S2). The presence of the same characteristic peaks (C═N, C═O, C-N) for TpBpy, Pd(II)-TpBpy and Pd-TpBpy membranes reveals that the formed COF layer is highly stable in acidic and reaction conditions. X-ray diffraction measurements of as-fabricated membranes show few measurable changes in their position but with a weak peak intensity possibly because the formed highly thin COF layer was strongly influenced by the PAN support. Elemental analyses of the membranes by using X-ray photoelectron spectroscopy characterization were conducted to determine their elemental compositions and the

oxidation state of palladium (Fig. S4). The narrow scan spectra of C 1 s for TpBpy AMs are deconvoluted into C─C, C═C, C─N, C═N, and C═O, confirming the successful synthesis of keto−enamine based TpBpy (Fig. S4c) [33]. The narrow scan spectra of O 1 s and N 1 s further confirm the formation of TpBpy AMs (Fig. S4d, e). In view of Pd (II)-TpBpy membranes, the narrow scan spectra of Pd 3d showed characteristic peaks at 337.2 eV and 342.5 eV, which correspond to the 3d$_{5/2}$ and 3d$_{3/2}$ states of Pd (II), respectively [34]. Of note, the XPS spectra of Pd(II)-TpBpy membranes exhibit the characteristic peak of Cl 2p (Fig. 2b, Fig. S4i), revealing successful capture of palladium by a TpBpy AM in the form of PdCl$_4^{2-}$. Importantly, the Pd 3d region of Pd-TpBpy membranes displays new characteristic peaks at 335.1 eV and 340.4 eV (Fig. 2c), corresponding to the 3d$_{5/2}$ and 3d$_{3/2}$ states of zero-valent Pd nanoparticles. However, two relatively weak peaks at 337.2 eV and 342.4 eV are ascribed to the 3d$_{5/2}$ and 3d$_{3/2}$ states of Pd (II) and PdO due to the insufficient reduction and inevitable surface oxidation. Surface elemental composition of palladium for Pd-TpBpy CMs is ca. 2.4 % determined by XPS analysis (Table S1). Thermal gravimetric analysis (TGA) curves of as-fabricated membranes in a nitrogen environment are plotted in Fig. S5. The residual weight (23.3 %) of Pd-TpBpy CMs is higher than that of TpBpy AMs (22.9 %), further confirming the presence of Pd nanoparticles within the AMs with a loading content of ca. 0.4 %. The permanent porous structure of the TpBpy active layer on the adsorptive membrane is crucial for the adsorption capacity. To access the porosity, the freestanding nanofilms fabricated at the aqueous/organic interface were collected for the N$_2$ sorption isotherm analysis at 77k (Fig. S6). Both nanofilms showcased a typical type-I isotherm, indicating a microporous structure of the active layers [35]. The BET surface areas of TpBpy and Pd-TpBpy nanofilm were 86.33 and 77.26 cm^2/g, respectively, calculated from the N$_2$ sorption isotherm (Table S3). A slight decrease in the surface area of Pd-TpBpy nanofilm is mainly induced by the occupation of Pd nanoparticles within the pores of a TpBpy nanofilm.

The surface morphology of the as-fabricated membranes was analyzed using scanning electron microscopy (SEM) images. The PAN surface has an abundance of pores, while TpBpy-COF membranes exhibit a more compact and uniform surface without visible defects (Fig. S7a,b). Atomic force microscopy (AFM) results also demonstrate a
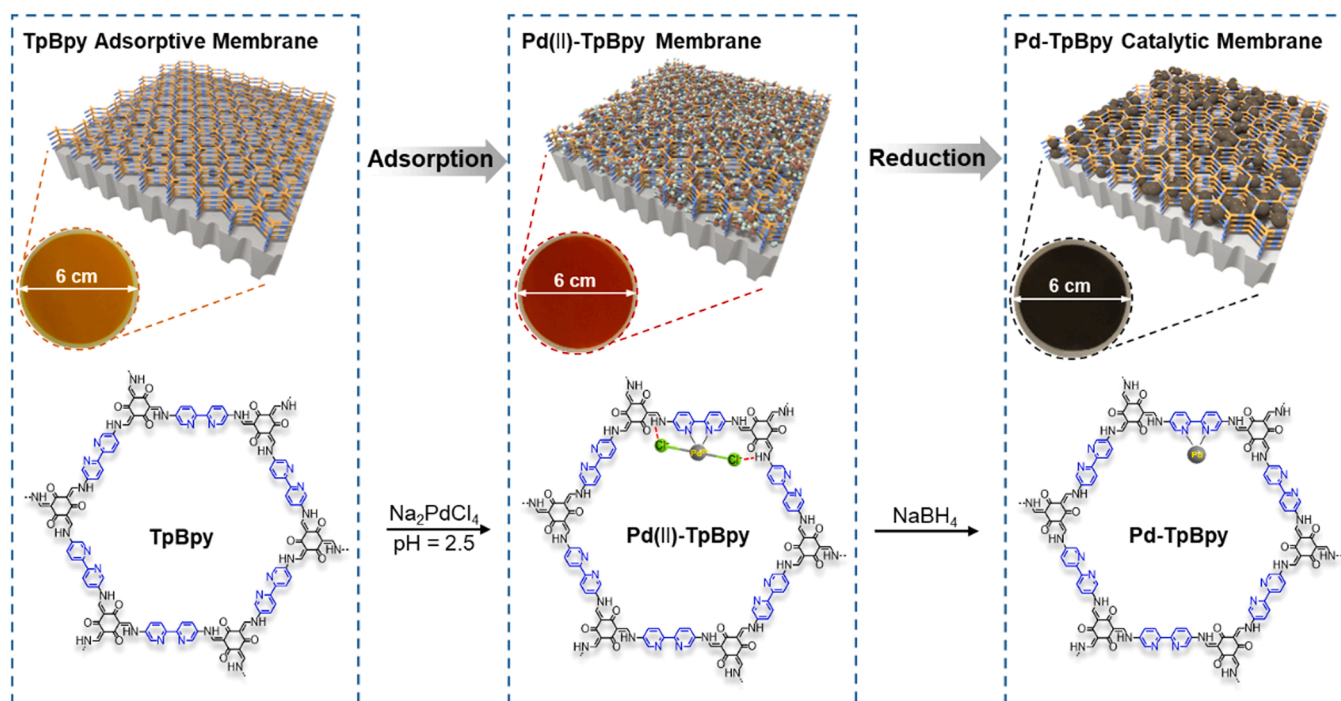

Fig. 1. Fabrication process and digital photos of a TpBpy adsorptive membrane, Pd(II)-TpBpy membrane, and Pd-TpBpy catalytic membrane.
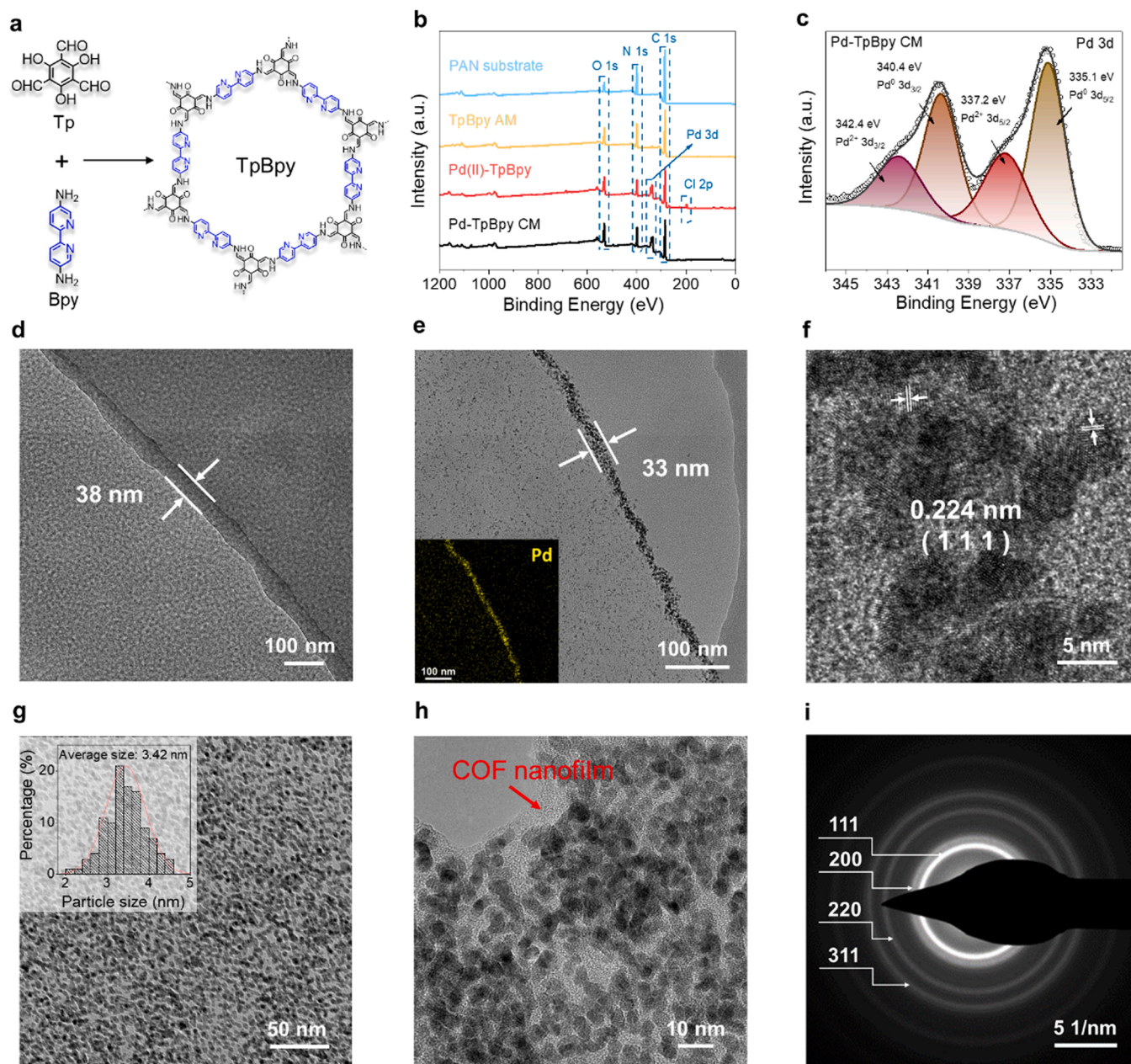
Fig. 2. Characterization of prepared membranes. (a) Synthesis and structure of the TpBpy. (b) XPS spectra of prepared membranes. The Pd 3d spectrum of (c) Pd-TpBpy CMs measured by XPS. The cross-sectional TEM image (d) of TpBpy AM. The cross-sectional TEM images (inset: element distribution map of Pd (yellow) in the Pd-TpBpy membrane) (e), cross-sectional high-resolution TEM image (f) of Pd-TpBpy CM. The surface Cryo-TEM images (g, h) of Pd-TpBpy film (inset of g: the size distribution profile of Pd nanoparticles). The selected area electron diffraction (SAED) pattern (i) of Pd-TpBpy film.

uniform AM surface with a low roughness (R_a = 8.06 nm, Fig. S8a). The transmission electron microscopy (TEM) images clearly present a 38-nm-thick and continuous TpBpy nanofilm (Fig. 2a, Fig. S10). By dissolving the underlying support, the resultant exfoliated TpBpy nanofilm is 37.8 ± 1.66 nm by AFM analyses (Fig. S8b,c), highly consistent with the TEM results. The high-angle annular dark-field STEM (HAADF-STEM) image and energy-dispersive X-ray spectroscopy (EDS) mapping of TpBpy AMs are displayed in Fig. S9c. The legible boundaries and an even elemental distribution confirm the uniform formation of a COF nanofilm at the top surface of the PAN support.

As bipyridine groups have a strong affinity to palladium, the possibility of using TpBpy AMs to capture palladium was explored. It is obvious that the TpBpy membrane surface turns from yellow to dark red after immersion in the acidic leaching liquor (Fig. S1). This is because the integration of palladium chlorate ion ($PdCl_n^{X-}$) with the TpBpy AMs

forms new chemical bonds of Pd-N [36]. The palladium contents in the AMs are precisely quantified by atomic absorption spectroscopy to be 5.6 wt%. The SEM images of the Pd(II)-TpBpy show a continuous and defect-free surface, demonstrating that the TpBpy AMs are highly resistant to acidic conditions (Fig. S7c). Due to strong binding interaction between bipyridine groups and $PdCl_n^{X-}$, we then explored the usage of TpBpy-COF membranes as template to confine the growth of palladium nanoparticles. The COF membrane with captured Pd(II) was in situ reduced using $NaBH_4$ in the mixed solvent of methanol and water, yielding a black Pd-TpBpy CM. The resultant Pd-TpBpy CMs also exhibit a uniform and intact surface with a low roughness of 9.5 nm (Figs. S7d, S8d). As shown in Fig. 2e, the TEM image of Pd-TpBpy CMs reveals the formation of 33-nm-thick films, in which an abundance of highly dispersed nanoparticles is present. This is highly consistent with results obtained by AFM analysis (34.1 ± 3.0 nm, Fig. S8e,f). Importantly, the

majority of ultrafine nanoparticles is distributed in the COF layer rather than on the surface. In addition, a small amount of the nanoparticles is distributed in the PAN support (Fig. 2e), mainly due to chemical affinity of cyano groups to palladium [37]. The high-resolution TEM image (HR-TEM) displays that the embedded nanoparticles have a crystal plane spacing of 0.224 nm corresponding to the (111) plane of Pd nanoparticles. Furthermore, the HAADF-STEM image in Fig. S10 shows a bright ultrathin recycled palladium layer, and the EDS mapping confirms the existence of Pd nanoparticles once again (Fig. 2e).

To further inspect the morphology and distribution of palladium nanoparticles in the COF layer, the Pd-TpBpy nanofilm was separated by dissolving the support prior to TEM analyses. Cryo-TEM can reduce the damage to the samples caused by the electron beam and thus avoid the deformation of the samples. The Cryo-TEM characterization provides visual evidence that the ultrafine Pd nanoparticles are uniformly distributed in the TpBpy-COF layer. (Fig. 2 g, Fig. S11). The Cryo-TEM image of Pd-TpBpy film also shows a crystal plane spacing of 0.224 nm, consistent with the results of HR-TEM (Fig. S11a). The corresponding selected area electron diffraction (SAED) pattern demonstrates that the polycrystalline ring corresponds to the (111), (200), (220), and (311) reflection planes of face-centered cubic Pd nanoparticles (Fig. 2i). These Pd nanoparticles uniquely evince an average size of 3.42 nm in diameter with a narrow size distribution (Fig. 2 g). Moreover, EDS mapping results demonstrate that C, N, O, and Pd are all uniformly distributed in the TpBpy-COF layer, further confirming the presence of highly dispersed Pd nanoparticles within the CMs (Fig. S12).

3.2. Adsorption performance of TpBpy adsorptive membrane

A membrane coupon (2 × 2 cm²) was soaked in an acidic solution (20 mL, pH = 2.5) to assess the effectiveness of TpBpy AM as a Pd(II) adsorbent. The impact of adsorption time on Pd(II) concentration of acidic feedwater is plotted in Fig. 3a and Fig. S13. The absorbance values were measured using a UV–vis spectrophotometer. It is evident that two

absorbance peaks at 207 and 236 nm markedly decrease when the adsorption attains an equilibrium state (Fig. S14). The lone pair electrons of N atoms from the pyridine of TpBpy-COF are protonated by hydrogen ions under acidic conditions. Fig. S15 shows that the TpBpy powder is positively charged at pH 2.5, which proves this conjecture. Since the predominant palladium species are in the form of $PdCl_3^-$ or $PdCl_4^{2-}$ at pH 2.5 [38], the anionic species are effectively adsorbed onto the TpBpy AMs surface based on strong electrostatic interactions. Due to the speciation of palladium that is affected by pH, the effect of pH value on Pd adsorption is shown in Fig. S16. The results reveal a marked increase of Pd adsorption capacity with pH increase from 0 to 3. This is because excessive chlorine ions at a lower pH compete strongly with the protonated anchoring sites of $PdCl_4^{2-}$. As the solution pH exceeds 3, the precipitation of palladium leads to the formation of $Pd(OH)^+/Pd(OH)_2$, rendering it inaccurate for measuring the adsorption capacity [38]. Furthermore, the uptake capacity shows a slight rise from 34.6 to 38.10 µg cm⁻² when the temperature increases from 15 °C to 55 °C, indicating that the adsorption of Pd(II) is an endothermic process (Fig. S17).

As exhibited in Fig. 3b, the uptake capacity attains up to 33.18 µg cm⁻² at equilibrium within 300 min, confirming a strong affinity of TpBpy-COF to Pd(II). To further understand the adsorption mechanism, the experimental kinetic data were fitted to a pseudo-second-order kinetic model using the following equation:

$$\frac{t}{Q_t} = \frac{t}{k_2 Q_e^2} + \frac{t}{Q_e} \tag{2}$$

where k_2 (cm² µg⁻¹ min⁻¹) is the rate constant of pseudo-second-order adsorption, Q_t (µg cm⁻²) is the adsorption amount of Pd(II) at time t (min), and Q_e (µg cm⁻²) is the adsorption amount of Pd(II) at equilibrium. The pseudo-second-order kinetic plot by linear regression shows a correlation coefficient (R^2) as high as 0.997, whereas the R^2 of linear regression of pseudo-first-order kinetic is only 0.687 (Fig. 3a, Fig. S18).
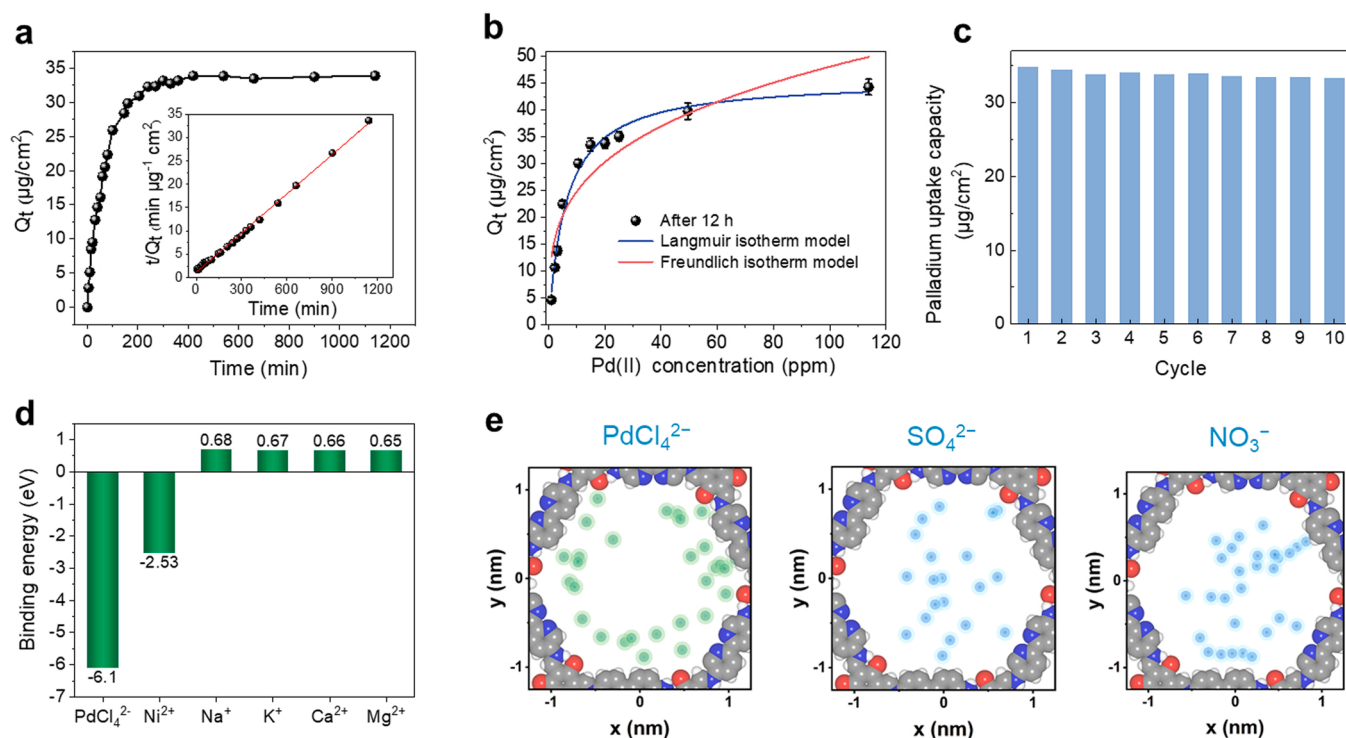

Fig. 3. Adsorption performance of TpBpy AMs. (a) Adsorption performance of TpBpy AMs, inset shows the pseudo-second-order kinetic plot for the adsorption. (b) Langmuir/Freundich adsorption isotherm curve. (c) The uptake capacity of Palladium for each adsorption and desorption cycle. (d) The adsorption energy between six metal ions and TpBpy by density functional theory (DFT) calculations. (e) Probability distribution of various anions in the TpBpy channel. Gray, red, and blue represent carbon, oxygen, and nitrogen, respectively.

The results illustrate that the interactions between TpBpy AMs and Pd (II) were primarily controlled by the chemical process. To explore the palladium uptake capacity of TpBpy AMs, equilibrium data were collected in terms of different palladium initial concentrations. The Langmuir/Freundlich adsorption isotherm curves are shown in Fig. 3c. The TpBpy AMs exhibit a very steep adsorption profile for Pd(II), indicating a very strong affinity to Pd(II). By comparing the correlation coefficients of the Langmuir model (0.999) and Freundlich model (0.847) determined by linear regression, the equilibrium adsorption data were better fitted with the Langmuir model (Fig. S19). Langmuir/ Freundlich adsorption isotherm model parameters of Pd(II) adsorption onto TpBpy AMs are provided in Table S2.

The recyclability of TpBpy AM was also explored; the result is shown in Fig. S20. The red Pd(II)-saturated TpBpy AM returns to its initial yellow after elution of palladium using the thiourea [39]. After ten cycles of adsorption and desorption, the inconspicuous decrease in adsorption capacity of palladium demonstrates the good reusability of TpBpy AM (Fig. 3c). Given that practical extrusion feedwater contains diverse ion species, we further evaluated the effectiveness of selectively capturing palladium from simulated leaching liquor. Fig. S21 shows the adsorption capacities of the TpBpy AMs toward different ions. It is evident that the TpBpy AMs attain a palladium uptake capacity of 32.3 μg cm^{-2} within 300 min, slightly lower than the adsorption capacity of a single-Pd(II) solution under identical contact time. Remarkably, the TpBpy AMs exhibit negligible uptake capabilities for Ni^{2+} and other competing ions like Na$^+$, K$^+$, Mg^{2+}, and Ca^{2+} (Fig. S21). Compared to the transition metals, the main group metals Na$^+$, K$^+$, Ca^{2+}, and Mg^{2+} have a weaker effect on the adsorption of palladium. Therefore, three transition metal cations were used to further investigate the effect on the selective recoverability of Pd(II). Fig. S22 showed that the adsorption capacities for Zn^{2+}, Cu^{2+}, and Fe^{3+} ions were much lower compared to palladium adsorption capacity, demonstrating an excellent Pd-selective recovery performance.

To better understand the palladium-pyridine interaction within the porous framework in acidic environment, the adsorption energy between metal ions and TpBpy was calculated by density functional theory (DFT, Fig. 3d, Fig. S23). Fig. S23a shows the model of the combination state between the TpBpy and Pd(II). The binding energy ($E_{binding}$) between Pd anion and TpBpy was calculated as − 6.10 eV, indicating that the metal ion has an affinity and stable adsorption structure with TpBpy [40]. By contrast, the positive binding energy for Na$^+$, K$^+$, Mg^{2+}, and Ca^{2+} indicates the repulsive force against TpBpy (Fig. S23b). A major reason lies in the electrostatic repulsion between the cations and the positively charged pyridine groups under acidic conditions. It is noted that the binding energy between Ni^{2+} and TpBpy was − 2.53 eV (Fig. S23c) due to local coordination interactions. While calculations proved that Ni^{2+} has a certain affinity with COF, simulating leaching liquor experiments the Ni^{2+} uptake capacity was much lower (Fig. S21) due to stronger affinity of TpBpy to palladium.

The leaching liquor also involves various anions with possibly competitive adsorption effects (such as SO$_4^{2-}$, NO$_3^-$, and Cl$^-$) in addition to metal ions. Hence, we performed all-atom molecular dynamics (MD) simulations to describe the molecular-level details of the specific adsorption behavior. Likewise, a theoretical calculation was performed to determine the group structure of pyridine under acidic conditions to simulate the acidic adsorption environment. Anion probability distributions (Fig. 3e, Fig. S24) within the TpBpy nanochannels were calculated to visualize the different interactions between anions and TpBpy. As shown in Fig. 3e, the PdCl$_4^{2-}$ shows an annular distribution nearby the channel wall, suggesting that PdCl$_4^{2-}$ is strongly attracted around the TpBpy. By contrast, the probability distributions show that SO$_4^{2-}$, NO$_3^-$, and Cl$^-$ are randomly distributed within the TpBpy channel, implying a weak affinity of TpBpy-COF to the anions under acidic conditions (Fig. 3e, Fig. S25). Accordingly, the selective adsorption of palladium is based on the combination of electrostatic attraction and coordination interaction.

3.3. Catalytic performance of Pd-TpBpy catalytic membrane

Based on the rarity and conspicuous catalytic properties of palladium, it is a sustainable and economic strategy to repurpose of palladium waste into catalytic membranes (CMs) using COF AMs for catalytic degradation of other toxic pollutants. Therefore, in situ growth of palladium nanoparticles within the AMs is explored to fabricate CMs via chemical reduction. As known, 4-Nitrophenol (4-NP) is a common nitrobenzene contaminant generated during manufacturing and material processing [41], which has an adverse effect on the environment and human health and is relatively stable in deep soil or groundwater [30]. In this scenario, the catalytic activity of the Pd-TpBpy CMs was assessed by the reduction of 4-NP using NaBH$_4$ as the reductant in a batch reactor. As evinced in Fig. 4a, either the introduction of only NaBH$_4$ or TpBpy AMs and NaBH$_4$ results in a minor decline in the absorption peak at 400 nm after 125 min, suggesting that their catalytic activity is insignificant. By contrast, when the CM coupon (2 × 2 cm^2) was introduced into the reaction system, time-dependent UV–visible spectra results show the sharp decrease of the 4-NP characteristic peak at 400 nm along with the emergence of a new adsorption peak at 300 nm (Fig. 4b). Furthermore, the 4-NP concentration gradually decreases with the extension of reaction time, and the conversion rate was calculated to be 96.5 % within 125 min (Fig. 4c). Fig. 4c inset further demonstrates the color change from bright yellow of 4-NP solution to transparent color of 4-AP solution. We also established the kinetics of the 4-NP reduction by following the intensity of the peak at 400 nm. The reaction is of first order in the concentration of 4-NP, and the apparent rate K_{cat} of catalysis is calculated by Eq. (3):

$$K_{cat} = -\frac{l(C_t/C_0)}{2a} = -\frac{ln\ A}{t} \qquad (3)$$

C_t is the concentration of 4-NP at reaction time t (min) and C_0 is the initial concentration of 4-NP. The plot of lnA=ln (C$_t$/C$_0$) versus the reaction time is shown in Fig. 4d. K_{cat} is calculated to be 2.65 × 10^{-2} min^{-1}, which is an order of magnitude higher than that for the reported CMs under the same experimental conditions [42]. Since the presence of organic matter has an adverse effect on the catalysis process, we further assessed the catalytic activity of the CMs in a simulated wastewater containing natural organic matter (humic acid, HA). In a static catalytic process (Fig. 5e), the conversion rate of 4-NP is 95.1 % after 125 min, only a 1.5 % decrease was observed compared to the HA-free system. Thus, we speculate that our reported CMs hold a promise for decontamination of practical wastewater.

Although the CMs show remarkable catalytic activity in static conditions, they indeed have insufficient contact with the reactants/reductants, and the batch reaction is not beneficial to continuous industrial water treatment. Thanks to the uniform and defect-free surface of the CMs, evenly distributed palladium nanoparticles within the COF layer, and high catalytic activity of palladium nanoparticles, it is anticipated that the CMs can achieve a superior performance in continuous flow catalytic reactions. Here we evaluated the liquid permeance and dynamic catalytic performance of the CMs using a cross-flow filtration system. After the penetration of feedwater through the CMs at 1.5 bar, the color of the permeate solution changes from bright yellow to colorless, and its absorption peak in the UV–visible spectrum disappears completely. The emergence of a new peak at 300 nm in the permeate solution demonstrates efficient catalytic degradation of 4-NP rather than the adsorption or rejection of 4-NP (Fig. 5a). More importantly, the CMs exhibit an ultrahigh conversion rate of 4-NP (99.9 %) with a remarkably high water permeability of 226.0 L m^{-2} h^{-1} bar^{-1} at 1.5 bar. Meanwhile, such a high water permeability can be maintained at different applied pressures (Fig. S26). Fig. 5b shows the 4-NP conversion at different pressures and feed flow rates, which could be maintained above 95 % when the pressure was doubled to 3 bar. The 4-NP conversion slightly decreased with the rise of 4-NP concentration at a constant NaBH$_4$ concentration. When the NaBH$_4$/4-NP ratio was fixed at
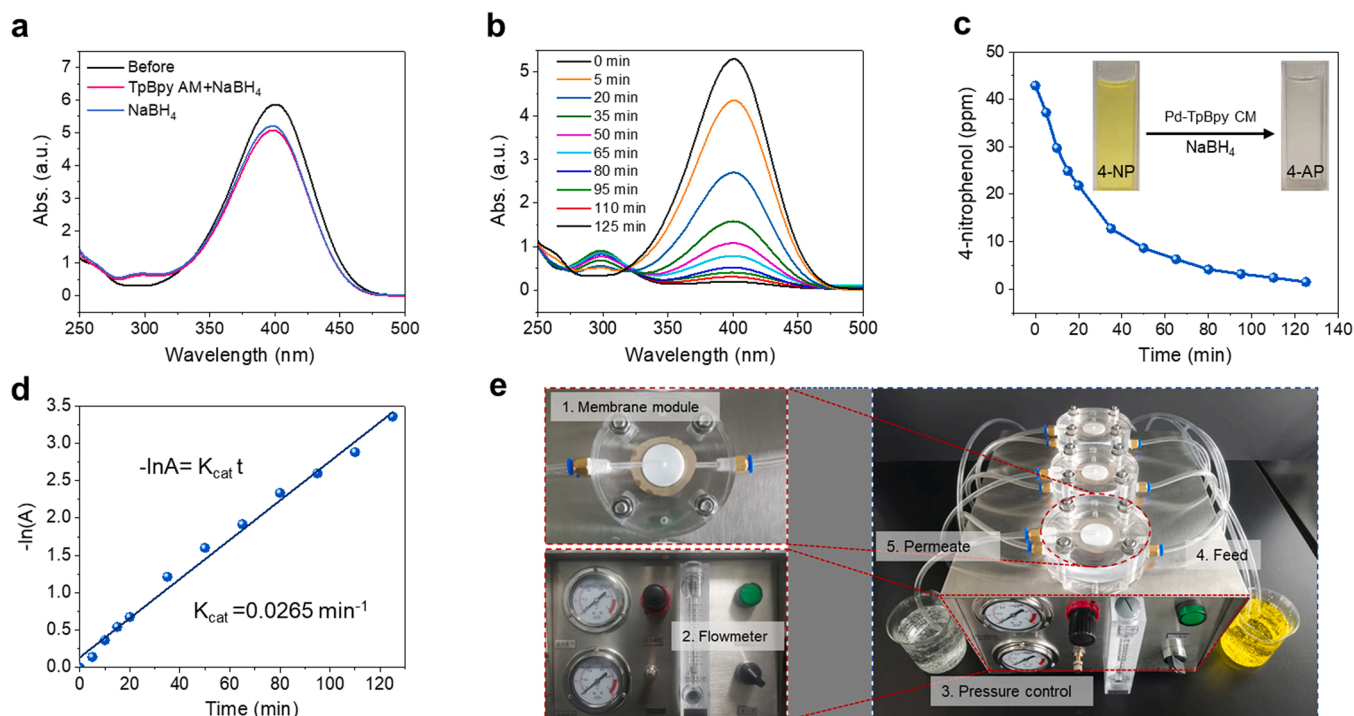
Fig. 4. Static catalysis performance of Pd-TpBpy CMs. (a) Control Experiments of TpBpy AM and NaBH₄ without Pd nanoparticles. (b) Time-dependent UV-Vis spectra of the reduction of 4-nitrophenol (4-NP) catalyzed by Pd-TpBpy CM in static catalytic experiments. (c) Plot of 4-NP concentration versus time (t), insets in b: solution color change before and after static catalysis. (d) Plot of -ln A (absorption at 400 nm) versus time (t) for the static catalysis of 4-NP, showing a first-order reaction. (e) Photos of a cross-flow device for continuous membrane catalysis.
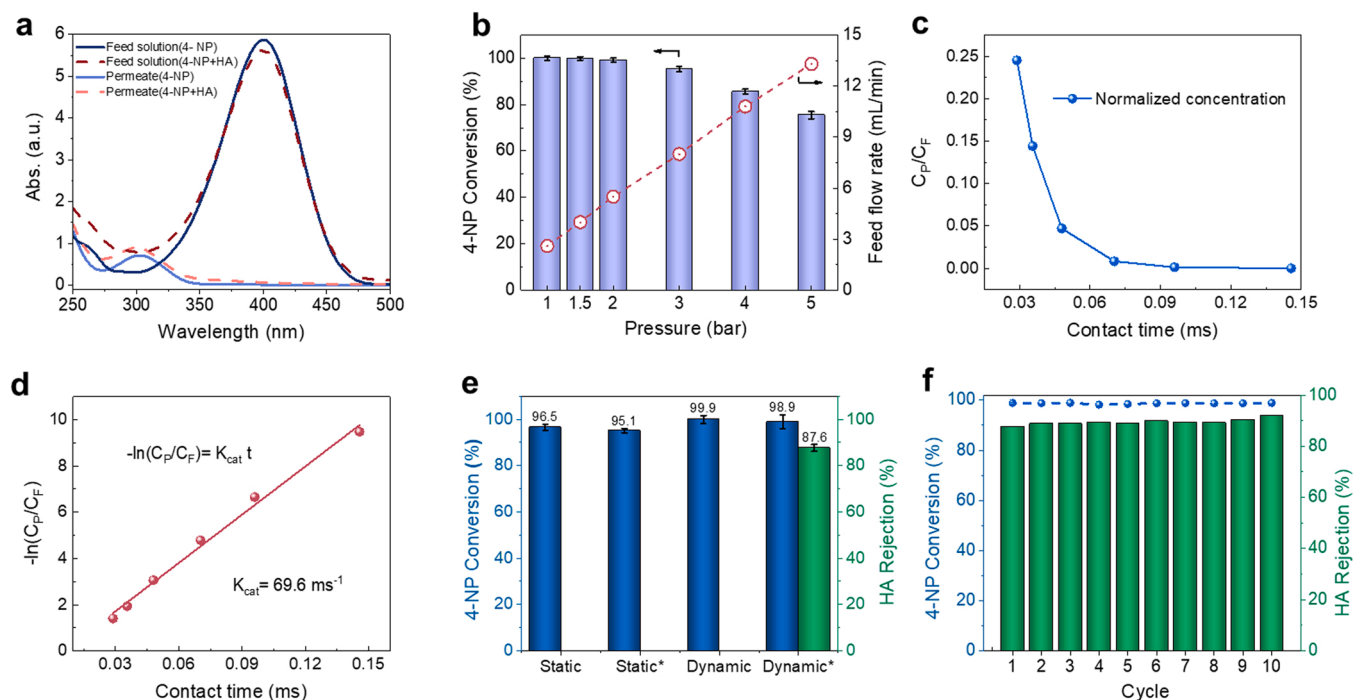

Fig. 5. Dynamic catalysis performance of Pd-TpBpy CMs. (a) UV-Vis spectra of feed solution and permeate before and after Pd-TpBpy CMs filtration in dynamic catalysis experiments. (b) The 4-NP conversion and feed flow rate under different pressure. (c) Normalized concentration of 4-NP (C_P/C_F) versus Pd-TpBpy CMs contact time. (d) Plot of -ln(C_P/C_F) versus Pd-TpBpy CMs contact time for the dynamic catalysis of 4-NP, showing a first-order kinetics. (e) Catalytic performance of the Pd-TpBpy CMs in static/dynamic catalytic experiments. Asterisks denotes a 4-NP aqueous solution containing HA. (f) Recyclability of the Pd-TpBpy CMs.

50: 0.3, the 4-NP conversion was maintained at a high and stable level in spite of threefold increment in the 4-NP concentration (Fig. S27). As known, the water flux of a membrane is associated with surface

hydrophilicity, which was evaluated by the water contact angle (WCA, Fig. S28). Both TpBpy and Pd-TpBpy membranes show comparably high hydrophilicity in contrast to hydrophilic PAN supports, facilitating a

high water permeability of a Pd-TpBpy CM. The molecular weight cut-off (MWCO) and pore size distribution were determined based on rejection of PEG or PEO with different molecular weight. As shown in the Fig. S29, the MWCOs of the PAN support, TpBpy AMs, and Pd-TpBpy CMs were 226.4, 19.6, and 84.5 kDa, respectively. Compared with TpBpy AMs, Pd-TpBpy CMs showed higher MWCO, pore size, and water permeability. During the reduction process, their contact with methanol as well as the formed bubbles could lead to partial swollen of PAN supports and weaken the interaction between Pd-COF layer and PAN supports, thus giving rise to an enhanced water permeability [43].

Because of the ultra-thin Pd-TpBpy nanofilm with highly dispersed and ultrafine Pd nanoparticles, the Pd-TpBpy CM produced an extremely short contact time of only 0.09 ms for the 99.9 % 4-NP conversion at 1.5 bar (Fig. 5c). Notably, the apparent rate constant K_{cat} of the dynamic catalysis was 4.17×10^6 min^{-1} (69.6 ms^{-1}, Fig. 5d), which is about 8 orders of magnitude faster than that of static catalysis (2.65×10^{-2} min^{-1}). Compared to static experiment, the dynamic catalysis breaks through the limitations of the thermodynamic equilibrium of traditional chemical reactions via rapid removal of the product (4-AP), thereby increasing the catalytic efficiency [44,45]. The K_{cat} of the dynamic catalysis is 4–6 orders of magnitude faster than those of other reported advanced catalytic membranes (2.4–386 min^{-1}, Table S5). The unprecedented catalytic efficiency is enabled by the small size and high reactivity of the Pd nanoparticles uniformly distributed in the ultrathin TpBpy layer. In addition, the dynamic catalysis of 4-NP solution that contains contaminant HA by using the CMs is shown in Fig. 5a, e. The results show that the conversion rate of 4-NP declines slightly to 98.9 % yet much higher than that in static condition. This is mainly because the high rejection of HA (87.6 %) benefits to reduce the adverse effect of HA and improves the catalytic performance.

In consideration of relistic recovery conditions, we further evaluated the catalytic performance of the CMs obtained by selective capture of palladium from simulated leaching liquor (Fig. S30). Both the 4-NP conversion and HA rejection have no noticeable changes in static/dynamic catalytic experiments compared to the CMs fabricated by using single Na$_2$PdCl$_4$ solution. This exciting result suggests that the recovery of palladium using COF AMs from leaching liquor for catalytic degradation of nitrobenzene contaminants is an achievable strategy. Recyclability and stability represent critical factors to evaluate a catalyst for practical applications. Thus, the dynamic catalysis and separation of HA-containing 4-NP solution by using the CMs were continuously repeated for 10 cycles, where both the catalytic efficiency and rejection maintain a high and stable level (Fig. 5 f). To further study the catalytic robustness and practicality of the Pd-TpBpy CM, a long-term experiment was carried out via the crossflow filtration device (Fig. S31). The results reveal that the water permeability of the catalytic membrane slightly reduced during 30 h continuous operation, but the high conversion of the contaminant (4-NP) could be well maintained. As shown in Fig. S32, the concentration of released palladium from Pd-TpBpy is as low as ~8.1 ppb after 72-hour release experiment, demonstrating that only 0.017 % of the palladium was released from the Pd-TpBpy. These results confirm a highly robust Pd-TpBpy structure with negligible losses of palladium nanoparticles.

The plausible mechanisms of synchronous separation and catalysis process were proposed in the presence of NaBH$_4$ and Pd-TpBpy CMs. The highly dispersed Pd nanopartilces from CMs play an important role to promote the electron transfer from the borohydride ions (BH$_4^-$) to the 4-NP. In detail, the 4-NP and BH$_4^-$ anions were adsorbed on the surface of Pd nanoparticles, facilitating the release of hydrogen radicals from the BH$_4^-$. The hydrogen radicals were subsequently transferred to the nitro group of 4-NP and thus lowered the activation energy barrier for 4-NP reduction [46,47]. The product 4-AP was eventually generated by replacing the oxygen in the nitro group to yield an amino group. In a pressure-driven dynamic catalytic process, the product 4-AP can rapidly permeate through the CMs and improve the reaction efficiency. Humic acid, serving as a common contaminant model in the wastewater, is

likely to be adsorbed on palladium surface and results in a reduced catalytic activity. Our reported CMs are effective for partial removal of humic acid and provide sufficient protection for the active sites of palladium. This synergistic sieving effect largely facilitates an ultrahigh catalytic activity in a continuous flow-through process, outperforming the state-of-the-art catalytic membranes (Table S5).

3.4. Antibacterial property

Membrane biofouling, broadly defined as the accumulation of microorganisms on the membrane surface, is a ubiquitous bottleneck that hinders water treatment efficiency induced by irreversible decline of water flux, augmented energy consumption, and shortened membrane lifespan [48,49]. Previous studies proved that Pd nanoparticles have favored antibacterial activities due to their high reactivity, particularly when the nanoparticle size is reduced substantially [50,51].

The antibacterial activities of as-fabricated membranes against the Gram-negative *Escherichia coli* (*E. coli*) are shown in Fig. 6, and Fig. S33. Both PAN support and TpBpy AMs have low antibacterial activity due to the absence of antibacterial segments. The palladium adsorption capacity of the TpBpy-AM with *E. coli* biofouling was tested to evaluate the negative effects of membrane biofouling. The uptake capacity of the TpBpy-AM with E. coli biofouling was decreased to 28.15 μg/cm^2, which is only 84.8 % of that of fresh membranes. In marked contrast, the Pd-TpBpy CMs exhibit superb antibacterial properties with the bacteriostasis rate (BR) as high as 98.1 % obtained by the plate-counting method (Fig. 6i). The well-supported hypothesis is that the generation of intracellular reactive oxygen species (ROS) induced by the palladium nanoparticles play a role in the bacteria inactivation (Fig. 6j) [52,53]. The experiment of palladium release indicated that a small number of palladium ions were released from the Pd-TpBpy CMs. The generated ROS from the released Pd ions plays a significant role in the bactericidal activity of as-fabricated CMs [54,55]. That is, an abundance of highly dispersed palladium nanoparticles with an ultrasmall average size (~3.42 nm) within the COF nanofilm accounts for such high antibacterial activity of the CMs. The SEM images of *E. coli* exposed to TpBpy AMs and Pd-TpBpy CMs are displayed in Fig. 6e-h. Most of the *E. coli* after contact with TpBpy AM show a rod-shaped shape with complete and smooth cell walls. However, the exposure of *E. coli* to the Pd-TpBpy CM causes their morphology to become wrinkled, and even shattered. It is noted that Pd nanoparticles induced cell lysis and loss of cell integrity, thus leading to DNA damage and protein denaturation [56].

Furthermore, the *Staphylococcus aureus* (*S. aureus*) was used as the Gram-positive bacterial model to explore the antibacterial activity of TpBpy AM and Pd-TpBpy CM. Compared to control *S. aureus*, the number of colonies was essentially unchanged after TpBpy AM treatment, whereas the number of colonies exposure to Pd-TpBpy CM substantially reduced (Fig. S34a-c). The obtained BR of Pd-TpBpy CM (96.3 %) is much higher than that of Pd-TpBpy AM (Fig. S34d). These excellent antimicrobial properties extend the usefulness of Pd-TpBpy CM in the treatment of real wastewater.

4. Conclusion

We propose a conceptual approach for repurposing palladium waste into catalytic membranes, using Pd-selective COF adsorptive membranes for environmental remediation. The use of bipyridine-containing COF membranes enables selective capture of precious palladium in the presence of other competing ions via local coordination and electrostatic interaction. Theoretical calculations demonstrate that the bipyridine in the COF exhibits a high strong affinity to Pd(II), yielding an annular Pd distribution along the TpBpy-COF nanochannel wall. Following Pd(II) capture, we converted the membrane into catalytic membranes, based on in situ Pd reduction to generate ultrafine palladium nanoparticles (~ 3.4 nm diameter, narrow size distribution) via confined growth. HR-TEM and cryo-TEM images reveal an abundance of highly dispersed
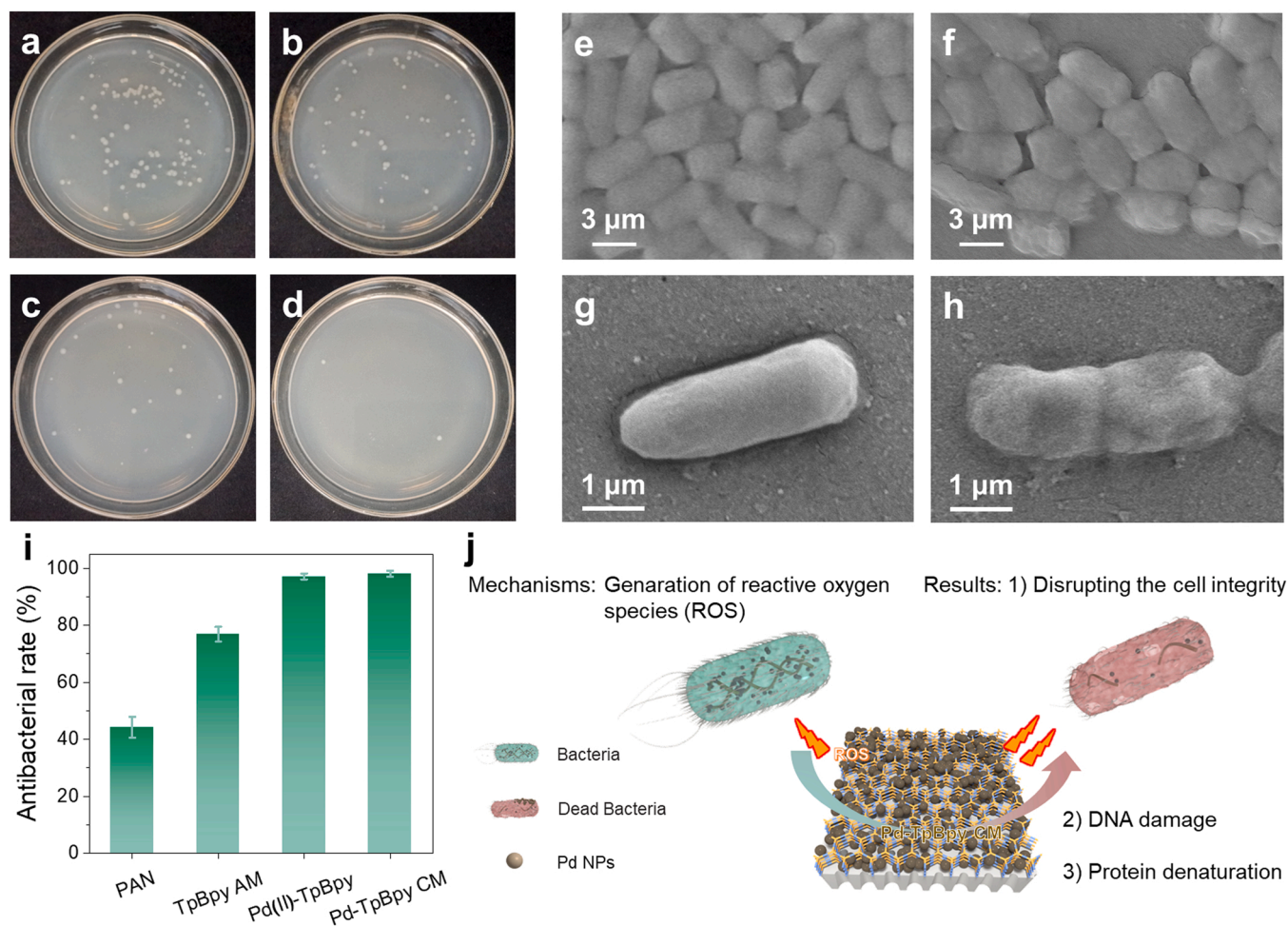
Fig. 6. Antibacterial activities and mechanism of prepared membranes. Antibacterial activities against *E. coli* of (a) control, (b) PAN substrate, (c) TpBpy AMs, (d) Pd-TpBpy CMs, based on the plate counting method. SEM images of *E. coli* exposed to TpBpy AMs (e, g) and Pd-TpBpy CMs (f, h). Antibacterial rates (i) and antibacterial mechanisms (j) of prepared membranes.

palladium nanoparticles within the thin COF layer, forming a 33-nm-thick, defect-free, catalytic palladium nanolayer. The resulting Pd-TpBpy catalytic membranes exhibit remarkably ultrahigh catalytic efficiency (99.9 %) and water permeability (226.0 L m^{-2} h^{-1} bar^{-1}) for the reduction of 4-nitrophenol in a continuous flow-through process. Endowed with sieving capability of COF membranes, the Pd-TpBpy CMs show superb catalytic degradation of 4-NP even when the humic acid is present in the feedwater. Moreover, the catalytic membranes show a superior antimicrobial activity (98.1 % against *E. coli* , 96.3 % against *S. aureus*), making these membranes promising for anti-biofouling and long-term usage in water decontamination. This sustainable strategy provides a new approach for recycling palladium waste, by fabricating multifunctional COF membranes that exhibit promising adsorptive, water transport, catalytic, and antimicrobial performances advantageous for water decontamination.

CRediT authorship contribution statement

Shaochong Cao: Investigation, Validation, Writing – original draft. **Dongyang Li:** Conceptualization. **Adam A. Uliana:** Writing – review & editing. **Yuanli Jiang:** Validation, Resources. **Junyong Zhu:** Funding acquisition, Conceptualization, Resources, Project administration, Supervision, Methodology, Writing – review & editing. **Yatao Zhang:** Funding acquisition, Conceptualization, Resources, Project administration, Writing – review & editing, Supervision. **Bart Van der Bruggen:** Validation, Writing – review & editing.

Declaration of Competing Interest

The authors declare that they have no known competing financial interests or personal relationships that could have appeared to influence the work reported in this paper.

Data availability

Data will be made available on request.

Appendix A. Supporting information

Supplementary data associated with this article can be found in the online version at doi:10.1016/j.apcatb.2022.122175.

References

[1] N. Xin, J. Guan, C. Zhou, X. Chen, C. Gu, Y. Li, M.A. Ratner, A. Nitzan, J. F. Stoddart, X. Guo, Concepts in the design and engineering of single-molecule electronic devices, Nat. Rev. Phys. 1 (2019) 211–230.

[2] M.S. Frei, C. Mondelli, R. García-Muelas, K.S. Kley, B. Puértolas, N. López, O. V. Safonova, J.A. Stewart, D. Curulla Ferré, J. Pérez-Ramírez, Atomic-scale engineering of indium oxide promotion by palladium for methanol production via CO_2 hydrogenation, Nat. Commun. 10 (2019) 3377.

[3] I.P. Mikheenko, J.A. Bennett, J.B. Omajali, M. Walker, D.B. Johnson, B.M. Grail, D. Wong-Pascua, J.D. Moseley, L.E. Macaskie, Selective hydrogenation catalyst made via heat-processing of biogenic Pd nanoparticles and novel 'green' catalyst for Heck coupling using waste sulfidogenic bacteria, Appl. Catal. B Environ. 306 (2022), 121059.

[4] Y. Liu, L. Zhang, Q. Song, Z. Xu, Recovery of palladium and silver from waste multilayer ceramic capacitors by eutectic capture process of copper and mechanism analysis, J. Hazard. Mater. 388 (2020), 122008.

[5] M.G. Campbell, D.C. Powers, J. Raynaud, M.J. Graham, P. Xie, E. Lee, T. Ritter, Synthesis and structure of solution-stable one-dimensional palladium wires, Nat. Chem. 3 (2011) 949–953.

[6] X. Huang, S. Tang, X. Mu, Y. Dai, G. Chen, Z. Zhou, F. Ruan, Z. Yang, N. Zheng, Freestanding palladium nanosheets with plasmonic and catalytic properties, Nat. Nanotechnol. 6 (2011) 28–32.

[7] Y.H. Huang, S.P. Yang, P.T. Lee, T.T. Kuo, C.E. Ho, Significant improvement of the thermal stability and electrochemical corrosion resistance of the Au/Pd surface finish through catalytic modification, Corros. Sci. 146 (2019) 112–120.

[8] C.R.M. Rao, G.S. Reddi, Platinum group metals (PGM); occurrence, use and recent trends in their determination, TrAC Trends Anal. Chem. 19 (2000) 565–586.

[9] Y. Chen, M. Xu, J. Wen, Y. Wan, Q. Zhao, X. Cao, Y. Ding, Z.L. Wang, H. Li, Z. Bian, Selective recovery of precious metals through photocatalysis, Nat. Sustain. 4 (2021) 618–626.

[10] P. Dato, Economic analysis of e-waste market, Int. Environ. Agreem. Politics Law Econ. 17 (2017) 815–837.

[11] S. Lin, Y. Zhao, J.K. Bediako, C.-W. Cho, A.K. Sarkar, C.-R. Lim, Y.-S. Yun, Structure-controlled recovery of palladium(II) from acidic aqueous solution using metal-organic frameworks of MOF-802, UiO-66 and MOF-808, Chem. Eng. J. 362 (2019) 280–286.

[12] P. Charlesworth, Separating the platinum group metals by liquid-liquid extraction, Platin. Met. Rev. 25 (1981) 106–112.

[13] Z. Hubicki, A. Wołowicz, A comparative study of chelating and cationic ion exchange resins for the removal of palladium (II) complexes from acidic chloride media, J. Hazard. Mater. 164 (2009) 1414–1419.

[14] G. Zhao, X. Huang, Z. Tang, Q. Huang, F. Niu, X. Wang, Polymer-based nanocomposites for heavy metal ions removal from aqueous solution: a review, Polym. Chem. 9 (2018) 3562–3582.

[15] J. Zhu, S. Yuan, J. Wang, Y. Zhang, M. Tian, B. Van der Bruggen, Microporous organic polymer-based membranes for ultrafast molecular separations, Prog. Polym. Sci. 110 (2020), 101308.

[16] M. Wang, P. Zhang, X. Liang, J. Zhao, Y. Liu, Y. Cao, H. Wang, Y. Chen, Z. Zhang, F. Pan, Z. Zhang, Z. Jiang, Ultrafast seawater desalination with covalent organic framework membranes, Nat. Sustain. (2022).

[17] X. Shi, Z. Zhang, S. Fang, J. Wang, Y. Zhang, Y. Wang, Flexible and robust three-dimensional covalent organic framework membranes for precise separations under extreme conditions, Nano Lett. 21 (2021) 8355–8362.

[18] H. Fan, A. Mundstock, A. Feldhoff, A. Knebel, J. Gu, H. Meng, J. Caro, Covalent organic framework–covalent organic framework bilayer membranes for highly selective gas separation, J. Am. Chem. Soc. 140 (2018) 10094–10098.

[19] J. Liu, G. Han, D. Zhao, K. Lu, J. Gao, T.-S. Chung, Self-standing and flexible covalent organic framework (COF) membranes for molecular separation, Sci. Adv. 6 (2020), eabb1110.

[20] M. Fan, W.D. Wang, Y. Zhu, X. Sun, F. Zhang, Z. Dong, Palladium clusters confined in triazinyl-functionalized COFs with enhanced catalytic activity, Appl. Catal. B Environ. 257 (2019), 117942.

[21] J.-Y. Yue, X.-L. Ding, Y.-T. Wang, Y.-X. Wen, P. Yang, Y. Ma, B. Tang, Dual functional sp2 carbon-conjugated covalent organic frameworks for fluorescence sensing and effective removal and recovery of Pd2+ ions, J. Mater. Chem. A 9 (2021) 26861–26866.

[22] S. Lu, Y. Hu, S. Wan, R. McCaffrey, Y. Jin, H. Gu, W. Zhang, Synthesis of ultrafine and highly dispersed metal nanoparticles confined in a thioether-containing covalent organic framework and their catalytic applications, J. Am. Chem. Soc. 139 (2017) 17082–17088.

[23] Y. Zhao, C. Xu, Q. Qi, J. Qiu, Z. Li, H. Wang, J. Wang, Tailoring delicate pore environment of 2D covalent organic frameworks for selective palladium recovery, Chem. Eng. J. 446 (2022), 136823.

[24] R. Tao, X. Shen, Y. Hu, K. Kang, Y. Zheng, S. Luo, S. Yang, W. Li, S. Lu, Y. Jin, L. Qiu, W. Zhang, Phosphine-based covalent organic framework for the controlled synthesis of broad-scope ultrafine nanoparticles, Small 16 (2020) 1906005.

[25] M. Hua, S. Zhang, B. Pan, W. Zhang, L. Lv, Q. Zhang, Heavy metal removal from water/wastewater by nanosized metal oxides: a review, J. Hazard. Mater. 211–212 (2012) 317–331.

[26] A.A. Uliana, N.T. Bui, J. Kamcev, M.K. Taylor, J.J. Urban, J.R. Long, Ion-capture electrodialysis using multifunctional adsorptive membranes, Science 372 (2021) 296–299.

[27] T.S. Vo, M.M. Hossain, H.M. Jeong, K. Kim, Heavy metal removal applications using adsorptive membranes, Nano Converg. 7 (2020) 1–26.

[28] Y. Deng, Z. Zhang, P. Du, X. Ning, Y. Wang, D. Zhang, J. Liu, S. Zhang, X. Lu, Embedding ultrasmall au clusters into the pores of a covalent organic framework for enhanced photostability and photocatalytic performance, Angew. Chem. Int Ed. Engl. 59 (2020) 6082–6089.

[29] Y.-J. Zhang, G.-X. Huang, L.R. Winter, J.-J. Chen, L. Tian, S.-C. Mei, Z. Zhang, F. Chen, Z.-Y. Guo, R. Ji, Y.-Z. You, W.-W. Li, X.-W. Liu, H.-Q. Yu, M. Elimelech, Simultaneous nanocatalytic surface activation of pollutants and oxidants for highly efficient water decontamination, Nat. Commun. 13 (2022) 3005.

[30] Z.I. Bhatti, H. Toda, K. Furukawa, p-Nitrophenol degradation by activated sludge attached on nonwovens, Water Res. 36 (2002) 1135–1142.

[31] B.A. Donlon, E. Razo-Flores, G. Lettinga, J.A. Field, Continuous detoxification, transformation, and degradation of nitrophenols in upflow anaerobic sludge blanket (UASB) reactors, Biotechnol. Bioeng. 51 (1996) 439–449.

[32] A.-J. Wang, H.-Y. Cheng, B. Liang, N.-Q. Ren, D. Cui, N. Lin, B.H. Kim, K. Rabaey, Efficient reduction of nitrobenzene to aniline with a biocatalyzed cathode, Environ. Sci. Technol. 45 (2011) 10186–10193.

[33] W.-R. Cui, C.-R. Zhang, W. Jiang, R.-P. Liang, J.-D. Qiu, Covalent organic framework nanosheets for fluorescence sensing via metal coordination, ACS Appl. Nano Mater. 2 (2019) 5342–5349.

[34] P. Pachfule, M.K. Panda, S. Kandambeth, S.M. Shivaprasad, D.D. Díaz, R. Banerjee, Multifunctional and robust covalent organic framework–nanoparticle hybrids, J. Mater. Chem. A 2 (2014) 7944–7952.

[35] S. An, Q. Xu, Z. Ni, J. Hu, C. Peng, L. Zhai, Y. Guo, H. Liu, Construction of covalent organic frameworks with crown ether struts, Angew. Chem. Int. Ed. 60 (2021) 9959–9963.

[36] P.B. White, S.S. Stahl, Reversible alkene insertion into the Pd-N bond of Pd(II)-sulfonamides and implications for catalytic amidation reactions, J. Am. Chem. Soc. 133 (2011) 18594–18597.

[37] Z. Wang, H. Zhang, L. Li, S. Miao, S. Wu, X. Hao, W. Zhang, M. Jia, Polyacrylonitrile beads supported Pd-based nanoparticles as superior catalysts for dehydrogenation of formic acid and reduction of organic dyes, Catal. Commun. 114 (2018) 51–55.

[38] Y. Ho Kim, Y. Nakano, Adsorption mechanism of palladium by redox within condensed-tannin gel, Water Res. 39 (2005) 1324–1330.

[39] Y. Bai, L. Chen, L. He, B. Li, L. Chen, F. Wu, L. Chen, M. Zhang, Z. Liu, Z. Chai, Precise recognition of palladium through interlaminar chelation in a covalent organic framework, Chem 8 (2022) 1442–1459.

[40] N. An, M. Zhao, X. Zheng, Q. Wang, X. Huang, B. Sun, Y. Shen, J. Wang, B. Chen, R. Liu, Synergistic oxytetracycline adsorption and peroxydisulfate-driven oxidation on nitrogen and sulfur co-doped porous carbon spheres, J. Hazard. Mater. 424 (2022), 127444.

[41] U. Chakraborty, G. Bhanjana, N. Kaur, R. Sharma, G. Kaur, A. Kaushik, G. R. Chaudhary, Microwave-assisted assembly of Ag2O-ZnO composite nanocones for electrochemical detection of 4-Nitrophenol and assessment of their photocatalytic activity towards degradation of 4-Nitrophenol and Methylene blue dye, J. Hazard. Mater. 416 (2021) 125771.

[42] X. Fang, J. Li, B. Ren, Y. Huang, D. Wang, Z. Liao, Q. Li, L. Wang, D.D. Dionysiou, Polymeric ultrafiltration membrane with in situ formed nano-silver within the inner pores for simultaneous separation and catalysis, J. Membr. Sci. 579 (2019) 190–198.

[43] M. Wu, J. Yuan, H. Wu, Y. Su, H. Yang, X. You, R. Zhang, X. He, N.A. Khan, R. Kasher, Z. Jiang, Ultrathin nanofiltration membrane with polydopamine-covalent organic framework interlayer for enhanced permeability and structural stability, J. Membr. Sci. 576 (2019) 131–141.

[44] J. Li, H. Yoon, T.-K. Oh, E.D. Wachsman, High temperature SrCe0.9Eu0.1O3−δ proton conducting membrane reactor for H2 production using the water–gas shift reaction, Appl. Catal. B Environ. 92 (2009) 234–239.

[45] S. Lotfi, K. Fischer, A. Schulze, A.I. Schäfer, Photocatalytic degradation of steroid hormone micropollutants by TiO2-coated polyethersulfone membranes in a continuous flow-through process, Nat. Nanotechnol. 17 (2022) 417–423.

[46] C.-S. Chen, T.-C. Chen, K.-L. Chiu, H.-C. Wu, C.-W. Pao, C.-L. Chen, H.-C. Hsu, H.-M. Kao, Silver particles deposited onto magnetic carbon nanofibers as highly active catalysts for 4-nitrophenol reduction, Appl. Catal. B Environ. 315 (2022), 121596.

[47] T.B. Nguyen, C.P. Huang, R.-a Doong, Enhanced catalytic reduction of nitrophenols by sodium borohydride over highly recyclable Au@graphitic carbon nitride nanocomposites, Appl. Catal. B Environ. 240 (2019) 337–347.

[48] J. Zhu, J. Hou, Y. Zhang, M. Tian, T. He, J. Liu, V. Chen, Polymeric antimicrobial membranes enabled by nanomaterials for water treatment, J. Membr. Sci. 550 (2018) 173–197.

[49] R. Zhang, Y. Liu, M. He, Y. Su, X. Zhao, M. Elimelech, Z. Jiang, Antifouling membranes for sustainable water purification: strategies and mechanisms, Chem. Soc. Rev. 45 (2016) 5888–5924.

[50] C.P. Adams, K.A. Walker, S.O. Obare, K.M. Docherty, Size-dependent antimicrobial effects of novel palladium nanoparticles, PLoS One 9 (2014), e85981.

[51] P. Makvandi, C.-y Wang, E.N. Zare, A. Borzacchiello, L.-n Niu, F.R. Tay, Metal-based nanomaterials in biomedical applications: antimicrobial activity and cytotoxicity aspects, Adv. Funct. Mater. 30 (2020) 1910021.

[52] G. Fang, W. Li, X. Shen, J.M. Perez-Aguilar, Y. Chong, X. Gao, Z. Chai, C. Chen, C. Ge, R. Zhou, Differential Pd-nanocrystal facets demonstrate distinct antibacterial activity against Gram-positive and Gram-negative bacteria, Nat. Commun. 9 (2018) 129.

[53] M.S. Al-Fakeh, S.O.M. Osman, M. Gassoumi, M. Rabhi, M. Omer, Characterization, antimicrobial and anticancer properties of palladium nanoparticles biosynthesized optimally using Saudi propolis, Nanomaterials 11 (2021) 2666.

[54] M. Polivkova, M. Valova, J. Siegel, S. Rimpelova, T. Hubáček, O. Lyutakov, V. Švorčík, Antibacterial properties of palladium nanostructures sputtered on polyethylene naphthalate, RSC Adv. 5 (2015) 73767–73774.

[55] M. Fernández-Arias, A.M. Vilas, M. Boutinguiza, D. Rodríguez, F. Arias-González, P. Pou-Álvarez, A. Riveiro, J. Gil, J. Pou, Palladium Nanoparticles synthesized by laser ablation in liquids for antimicrobial applications, Nanomaterials 12 (2022) 2621.

[56] E. Dahal, J. Curtiss, D. Subedi, G. Chen, J.P. Houston, S. Smirnov, Evaluation of the catalytic activity and cytotoxicity of palladium nanocubes: the role of oxygen, ACS Appl. Mater. 7 (2015) 9364–9371.